JOURNAL OF GEOPHYSICAL RESEARCH, VOL. 94, NO. C2, PAGES 2045–2056, FEBRUARY 15, 1989

The Decay of Wind-Forced Mixed Layer Inertial Oscillations Due to the β Effect

ERIC A. D'ASARO

Applied Physics Laboratory and School of Oceanography, College of Ocean and Fishery Sciences, University of Washington, Seattle

Wind generation of mixed layer near-inertial frequency oscillations has been observed and successfully modeled many times. Modeling of the decay of these currents by linear wave theory has been more difficult because the necessary horizontal scales are much smaller than the typical horizontal scales of the wind. A new, and highly effective, mechanism for generating such scales by the β effect is proposed here. An asymptotic analysis of the linear equations is presented which suppresses high-frequency gravity waves and thus simplifies the near-inertial frequency dynamics. The computed residence time for inertial motions in the mixed layer depends both on the scales of the wind and on β, with β imposing an upper limit of 1–2 weeks. The relative importance of the wind and β is estimated using realistic wind stress fields, generated by advecting Seasat scatterometer data over the simulated ocean. The predicted horizontal scales and decay times of mixed layer inertial motions are similar to those observed. The subsynoptic scales of the wind, the advection speed, and β are all important in determining the decay time of the simulated mixed layer inertial currents.

1. INTRODUCTION

Near-inertial oscillations are an important velocity component in the upper ocean, commonly contributing half or more of the kinetic energy and a somewhat smaller fraction of the 10-m shear [*D'Asaro*, 1985*b*]. They play a key role in theories of mixed layer deepening [*Niiler and Kraus*, 1977; *Price*, 1981] and have been observationally linked with patches of enhanced mixing [*Kunze and Lueck*, 1986; *Gregg et al.*, 1986; *Marmorino et al.*, 1987]. Under some circumstances they may be sufficiently nonlinear to generate wave-forced and Stokes flows of several centimeters per second [*Price*, 1983; *White*, 1986].

Webster [1968] and *Pollard and Millard* [1970] were the first of numerous investigators to report the generation of energetic near-inertial frequency oscillations in the mixed layer during storms. *Pollard and Millard* [1970] introduced the following simple model of the generation process:

$$\frac{\partial u}{\partial t} - fv = \frac{\tau_x}{\rho_0 H} - ru \tag{1}$$

$$\frac{\partial v}{\partial t} + fv = \frac{\tau_y}{\rho_0 H} - rv \tag{2}$$

where the velocity components u and v in a uniform surface mixed layer of depth H and density ρ_0 are driven by a wind stress $\boldsymbol{\tau} = (\tau_x, \tau_y)$ and decay through the action of an arbitrary decay constant r. With $r = 0$, these equations are valid for a rapidly varying wind under the same conditions that an Ekman layer exists for a slowly varying wind [*Gill*, 1982, section 9.3]. Like the Ekman equations, this model has been successful in explaining a large number of observations. Some recent examples of its application are given by *Sherwin* [1987] and *Paduan et al.* [1988] (see *D'Asaro* [1985*a*] for more examples).

The greatest weakness of (1) and (2) is the arbitrary decay constant r. Observed mixed layer inertial oscillations clearly decay within a week or so after their generation, corresponding to r^{-1} values between 2 and 20 days. Linear theory has often been used to explain this decay, starting with *Pollard* [1969], with recent work by *Price* [1983], *Gill* [1984], *Greatbatch* [1984], and *Kundu* [1986], among others. Although definitive verification of these theories is still lacking, limited comparisons with data are encouraging [*Price*, 1983; *D'Asaro*, 1985*b*; *Kundu and Thompson*, 1985; *Sanford et al.*, 1987].

A typical result is that of *Gill* [1984] (hereinafter referred to as G84), who finds that significant decay of mixed layer inertial currents will occur in time

$$t_1 = \frac{\pi f}{k^2 c_1^2} \tag{3}$$

where c_1 is the phase speed of the first baroclinic internal mode and k is the horizontal wave number of the mixed layer inertial motions imposed by the wind stress. Typically, the wind stress has horizontal scales of many hundreds of kilometers [*Freilich and Chelton*, 1986]. For a typical value of $c_1 = 2.7\,\mathrm{m\,s^{-1}}$ [G84] and $k = (500\,\mathrm{km})^{-1}$, t_1 is about 4 months. This is at least an order of magnitude larger than observed t_1. Conversely, if significant decay is to occur within a few inertial periods, as was found, for example, by *D'Asaro* [1985*a*], k^{-1} must clearly be smaller than 100 km. The few existing observations suggest that wind-forced near-inertial motions have horizontal scales consistent with the linear theory [*D'Asaro*, 1985*a*; *Kundu and Thompson*, 1985]. We are thus faced with a dilemma: How does the wind stress field with a typical scale of hundreds of kilometers generate near-inertial motions that are horizontally much smaller?

There are several possible solutions to this dilemma, within the framework of linear wave theory. First, small-scale fluctuations in wind stress do exist in the atmosphere. Hurricanes, which often have a radius of less than 100 km, are a prime example. For such storms, *Price* [1983], *Greatbatch* [1984], and *Sanford et al.* [1987] find excellent agreement with observations. Mid-latitude storms also have considerable small-scale structure [*Houze and Hobbs*, 1982; *Overland and Wilson*, 1984]. *D'Asaro* [1985*b*] used equations (1) and (2) with mid-latitude wind data to show that the generation of mixed layer near-inertial oscillations usually corresponds to the passage of a small-scale atmospheric feature, such as a front or small low. Such features may have a characteristic scale much less than typical synoptic systems and thus

Paper number 88JC03890.
0148-0227/89/88JC-03890$05.00

induce a more rapid decay of the associated inertial oscillations.

Second, small-scale wind stress patterns typically translate over the ocean with a speed C of the order of 10 m s^{-1}. This introduces a horizontal scale $Cf^{-1} \approx 100$ km, the distance the wind stress pattern or "storm" travels in a time f^{-1}. This is also much smaller than the typical scale of synoptic systems and thus yields a decay time for mixed layer inertial oscillations much closer to that observed. *D'Asaro* [1985*a*] and *Kundu and Thompson* [1985] invoke this advection mechanism to produce the small scales necessary to model observations of near-inertial energy transfer from the mixed layer to the thermocline.

In this article a third mechanism for generating small horizontal scales in mixed layer inertial oscillations is proposed. It relies only on the latitudinal variation of f, the β effect, and thus does not depend on any particular characteristic of the wind stress field. Suppose that mixed layer inertial currents of very large horizontal scale are generated by the wind stress. The subsequent evolution of these currents, assuming no subsequent wind generation, can be described by

$$u + iv = \tilde{U}e^{-ift} \tag{4}$$

which is an exact solution to (1) and (2) with $\tau = 0$, $r = 0$, and f constant. If instead $f = f_0 + \beta y$,

$$u + iv = \tilde{U}e^{-if_0t - i\beta yt} \tag{5}$$

In this latter case, the inertial oscillations have a north-south wave number βt. At 50°N this equals (100 km)$^{-1}$ for $t = 6.6$ days. In this way inertial oscillations of arbitrarily large initial scale will, within a week or so, develop scales small enough to transfer energy efficiently to the thermocline by linear dynamics.

In this paper, the relative importance of these three mechanisms will be explored using theory and realistic wind stress fields. In section 2, a multiple time scale analysis of the linear equations of motion is presented that yields a general expression (equation (35)) for the evolution of near-inertial motions on a β plane. In section 3 this is applied to determining a time scale for the decay of mixed layer inertial oscillations by each of the three mechanisms described above. In section 4, the relative importance of the three mechanisms is addressed using wind stress fields derived from Seasat microwave scatterometer data, which can resolve 100-km-scale fluctuations in the wind field. Sections 5 and 6 are a summary and discussion of these results.

2. A LINEAR MODEL OF INERTIAL FREQUENCY DYNAMICS

A set of equations describing the linear evolution of near-inertial frequency internal gravity waves is derived below using an asymptotic perturbation analysis that is uniformly valid in time. Many aspects of this analysis will draw upon G84. Readers who are uninterested in theoretical details may wish to skip to section 2.5 for a physical discussion of the results.

2.1. *Equations of Motion*

Consider the linear, Boussinesq, β plane, hydrostatic equations for a flat-bottomed ocean of depth B, mixed layer depth H, and buoyancy frequency profile $N(z)$ [G84]. Here y is north, x is east, and z is up. The system is forced by a wind stress $\tau = (\tau_x, \tau_y)$ modeled as a body force with a depth distribution $Z(z)$:

$$u_t - fv = -P_x + \frac{\tau_x}{\rho_0 H} Z(z) + \beta yv \tag{6}$$

$$v_t + fu = -P_y + \frac{\tau_y}{\rho_0 H} Z(z) - \beta yu \tag{7}$$

$$N^2 w = -P_{zt} \tag{8}$$

$$u_x + v_y + w_z = 0 \tag{9}$$

where the reference density ρ_0 has been absorbed into the pressure, P. Previous studies have shown distinctly different responses for the barotropic and baroclinic modes [G84]. We are interested in the baroclinic response in this study and will therefore use rigid lid boundary conditions

$$w(0) = w(-B) = 0 \tag{10}$$

Following G84, the wind stress will be distributed uniformly over the mixed layer so that

$$\begin{aligned} Z(z) &= 1 + H/B \quad & z > -H \\ Z(z) &= H/B \quad & z < -H \end{aligned} \tag{11}$$

where the first term ensures that there is no projection on the barotropic mode.

We will derive a general solution to (6)–(11) assuming a horizontally homogeneous stratification, i.e., H and N^2 are functions only of z, for variations in $\tau(x, y, t)$ of horizontal scales sufficiently large that high-frequency gravity waves are not excited.

2.2. *Vertical Structure*

Equations (8)–(10) can be combined to form

$$P_t = \mathbf{I}\nabla_{\mathbf{H}} \cdot \mathbf{u} \tag{12}$$

where $\nabla_{\mathbf{H}} \cdot \mathbf{u} = u_x + v_y$.

$$\mathbf{I} = (1 - M) \int_{-B}^{z} dz' N^2(z') \int_{-B}^{z'} dz'' \tag{13}$$

is an integral operator that combines (8) and (9), and

$$M = \frac{1}{B} \int_{-B}^{z} dz \tag{14}$$

is an integral operator required by (10). In (12) the operator $\mathbf{I}$ integrates w_z to find w and then applies (8) to find the resulting pressure field as discussed in section 3.2.1.

An alternative [G84] to using the integral operator $\mathbf{I}$ is to make a modal decomposition, i.e., find the eigenfunctions p_n with corresponding phase speed c_n that satisfy

$$\mathbf{I} p_n = -c_n^2 p_n \tag{15a}$$

or equivalently

$$c_n^2 \left[\frac{d}{dz} \frac{1}{N^2} \frac{d}{dz} \right] p_n = p_n \tag{15b}$$

with boundary conditions (10). The solution is then expanded in terms of these modes:

$$U(x, y, z) = \sum_{n=1}^{\infty} \sigma_n p_n(z) U_n(x, y) \tag{16}$$

Here, this expansion is delayed until a general space-time solution is obtained.

2.3. *Nondimensionalization*

Assuming velocity, vertical, horizontal, and time scales V, D, L, and f^{-1}, respectively, gives the nondimensional forms of (6), (7), and (12):

$$u'_{t'} = v' - \varepsilon P'_{x'} + T_x Z(z') + \varepsilon\delta y' v' \tag{17}$$

$$v'_{t'} = -u' - \varepsilon P'_{y'} + T_y Z(z') - \varepsilon\delta y' u' \tag{18}$$

$$P'_{t'} = \mathbf{I}'\nabla'_H \cdot \mathbf{u}' \tag{19}$$

where

$$\varepsilon = \frac{g\,\Delta\rho D}{\rho_0 f^2 L^2} \tag{20}$$

$$\delta = \frac{\beta L}{f\varepsilon} \equiv \frac{L}{R\varepsilon} \tag{21}$$

$$\frac{g\,\Delta\rho}{\rho_0} = \int_{-B}^{0} N^2 dz \tag{22}$$

$\mathbf{T} = \boldsymbol{\tau}/(\rho_0 H\, Vf)$ and $\beta = fR^{-1}$. The prime denotes dimensionless variables. $\mathbf{I}$ and P are nondimensionalized by $g\,\Delta\rho Z/\rho_0$ and $fLU\varepsilon$, respectively.

Equations (17) and (18) can be combined by defining a complex velocity $U' = u' + iv'$ and wind stress forcing $F = T_x + iT_y$. The nondimensional equations are then

$$U'_{t'} + iU' = -\varepsilon(P'_{x'} + iP'_{y'}) - i\,\varepsilon\delta y' u' + FZ'(z') \tag{23}$$

$$P'_{t'} = \tfrac{1}{2}\mathbf{I}'\left[U'_{x'} + U'^{*}_{x'} - i(U'_{y'} - U'^{*}_{y'})\right] \tag{24}$$

where the asterisk denotes complex conjugation. This complex number technique is used to clarify the exposition. It can, at times, result in wrong answers, but it does not do so in any of the results presented here.

Two nondimensional parameters appear in (23) and (24). The first, ε, is the squared ratio of the Rossby radius to the scale of the motion. This must be small if the linear response is to be dominated by motions with a frequency close to f [G84]. With $\varepsilon = 0$, for example, (23) is equivalent to an undamped version of (1) and (2). The second, $\varepsilon\delta$, is the ratio of the scale of the motion to $R = f\beta^{-1}$. Since R (7600 km at 50°N) is comparable to the radius of the Earth, $\varepsilon\delta$ is also small. It is not negligible, however.

2.4. *Asymptotic Analysis*

We will derive an approximation to (23) and (24) that is asymptotically valid at all times for small ε and $\varepsilon\delta$ using the method of multiple time scales [*Kervorkian and Cole*, 1981]. This derivation is inspired by *Hasselman* [1970], is similar to that of *Smith* [1973], and also expands on some results of *D'Asaro* [1985*a*]. We expand U and P in a perturbation expansion

$$U = U_0(t'', \tau'') + \varepsilon\, U_1(t'', \tau'') + \cdots \tag{25}$$

where $t'' = t'[1 + O(\varepsilon^2)]$ and $\tau'' = \varepsilon t'$ are "fast" and "slow" time variables, respectively. The equations are expanded in orders of ε, with the τ'' equation chosen so as to eliminate resonance.

The resulting solution to order ε is

$$U' = U'_E + \left[\tilde{U}'_F(t'')Z'(z') + \tilde{U}'(\tau'', z')\right]e^{-it''}$$

$$+\varepsilon\tilde{U}'_1(z', \tau'')e^{it''} \tag{26}$$

where

$$U'_E = -iFZ'(z') \tag{27}$$

$$\tilde{U}'_F = \int_0^t i\frac{\partial' F}{\partial t''}\, e^{it}\, dt \tag{28}$$

$$\frac{\partial\tilde{U}'}{\partial\tau''} = -(\tfrac{1}{2}i\mathbf{I}'\nabla'^2_H + i\,\delta y')\left[\tilde{U}' + \tilde{U}'_F Z'(z')\right] \tag{29}$$

$$\tilde{U}'_1 = \tfrac{1}{4}\mathbf{I}'\left[\frac{\partial^2}{\partial x'^2} - \frac{\partial^2}{\partial y'^2} + 2i\frac{\partial^2}{\partial x'\partial y'}\right][\tilde{U}'^{*} + \tilde{U}'^{*}_F Z'(z')] \tag{30}$$

$$\frac{\partial U'_G}{\partial t''} + iU'_G = \mathbf{I}'Z'(z')\left[\frac{\partial'}{\partial x'} + i\frac{\partial'}{\partial x}\right]$$

$$\times\left[\nabla'_H\cdot\mathbf{T}' + \int_0^{t''}\hat{\mathbf{z}}'\cdot\nabla'_H\times\mathbf{T}'\,dt\right] - i\,\delta y' U'_G \tag{31}$$

or dimensionally

$$U = U_E + \left[\tilde{U}_F(t)Z(z) + \tilde{U}(t, z)\right]e^{-ift} + \tilde{U}_1 e^{ift} + U_G \tag{32}$$

$$U_E = \frac{i}{fH\rho_0}(\tau_x + i\tau_y)Z(z) \tag{33}$$

$$\tilde{U}_F = \int_0^t ie^{ift}\frac{\partial}{\partial t}\left[\frac{\tau_x + i\tau_y}{\rho_0 H}\right]dt \tag{34}$$

$$\tilde{U}_t = -\frac{i}{2f}\mathbf{I}\nabla^2_H(\tilde{U} + \tilde{U}_F Z) \tag{35}$$

$$\tilde{U}_1 = \frac{1}{4f^2}\mathbf{I}\left[\frac{\partial^2}{\partial x^2} - \frac{\partial^2}{\partial y^2} + 2i\frac{\partial^2}{\partial xy}\right](\tilde{U}^{*} + \tilde{U}^{*}_F Z) \tag{36}$$

2.5. *Inertial Motion Dynamics*

The velocity field described by (32) is the sum, from left to right, of "Ekman" velocities U_E; inertial frequency oscillations with components $\tilde{U}_F$, $\tilde{U}$, and U_1; and geostrophic and other noninertial forced motions U_G. Each of these terms is discussed, in turn, below. Notably, high-frequency internal waves do not appear here; they have been filtered from the equations of motion by the perturbation analysis. Accordingly, the equations contain only one time derivative, as opposed to the full equations (6)–(10) or G84's equation (3.9), which contain second derivatives. This makes the new equations simpler to analyze or numerically integrate.

2.5.1. *Directly forced Ekman and inertial velocities.* The first two terms in (32) represent motions directly forced by the wind stress in the mixed layer. These motions are the solution to (6) and (7) for infinite horizontal scale ($\varepsilon = 0$), or equivalently (1) and (2) with $r = 0$. The general solution to these equations consists of two terms. The well-known Ekman flow U_E is directly proportional to the wind stress, but at right angles to it, as is indicated by the complex right-hand side of (33). In addition, the time dependent part of the wind stress induces an inertially oscillating velocity whose amplitude $\tilde{U}_F$ depends on past values of the inertially oscillating component of the wind stress (equation (34)). Wind-forced motions in the mixed layer have been successfully modeled by these two terms many times, as discussed in the introduction.

2.5.2. *Propagating inertial motions.* The propagation of inertial motions is described by (35). The formulation here differs from that used previously (however, see *Smith* [1973]) in that it explicitly gives the evolution of the complex inertial magnitude $\tilde{U}$ as a function of its current value and the forcing. Observations of near-inertial motions are commonly expressed in terms of the space and time variation of $\tilde{U}$ [*Pollard*, 1980; *Weller*, 1982; *D'Asaro*, 1985*a*]. Here we see that the time derivative of $\tilde{U}$ depends on the values of $\nabla^2_H\,\tilde{U}$ over the entire water column. The operator $\mathbf{I}$ describes the contribution of the values at various depths (see section 3.2 for discussion). Equation (35) thus explicitly describes what space-time measurements are necessary for locally testing a linear description of near-inertial frequency dynamics.

The formulation used here is, of course, equivalent to other descriptions of linear dynamics. If a modal expansion (equation (16)) is substituted into (35) with $\tilde{U}_F = 0$, the resulting equation describes the evolution for a single modal coefficient $\tilde{U}_n$

$$\frac{\partial \tilde{U}_n}{\partial t} = \frac{i}{2f} c_n^2 \nabla_H^2 \tilde{U}_n \tag{37}$$

An f plane dispersion relation is derived by substituting $\tilde{U}_n e^{ift} = \hat{U} e^{ikx + ily - i\omega t}$ into (37) with $\beta = 0$, yielding

$$\omega - f = \frac{c_n^2}{2f}(k^2 + l^2) \tag{38}$$

This is identical to the full internal wave dispersion relation [G84, equation (4.3)] if the approximation

$$\omega^2 - f^2 \approx 2f(\omega - f) \tag{39}$$

is made. Thus the asymptotic approximations used here are, for internal waves, equivalent to assuming that the wave frequency is close to f. Any dynamics associated only with higher-frequency internal waves has been eliminated.

The second term in expression (35) adds the β effect to the evolution equation. Assuming a modal expansion and $\tilde{U}_n e^{-ift} = \hat{U}_n(y) e^{ikx - i\omega t}$ gives an equation for the latitudinal variation of $\hat{U}_n$:

$$\frac{\partial^2 \hat{U}_n}{\partial y^2} + \frac{2f}{c_n^2}\left[(\omega - f - \beta y) - k^2\right]\hat{U}_n = 0 \tag{40}$$

This is a variant on the usual equation for wave propagation on a β plane [*Munk*, 1980; *Fu*, 1981]. A turning point occurs at the latitude for which the bracketed quantity is zero. Freely propagating waves cannot travel north of this latitude.

2.5.3. *Asymmetries in inertial motions.* The horizontal velocity vector for a sinusoidal propagating near-inertial wave on an f plane does not move in an exact circle but moves in an ellipse whose major axis is aligned along the wave number. The ratio of major to minor axis is equal to ωf^{-1} [*Calman*, 1978]. Here, this same asymmetry is expressed by the small anticlockwise rotating inertial velocity U_1 (equation (36)). Substituting a modal expansion in (36) and assuming $\tilde{U}_n e^{-ift} = \hat{U}_n e^{i\alpha(x\cos\theta + y\sin\theta) - i\omega t}$ yields

$$\hat{U}_{n1} = \frac{c_n^2 \alpha^2}{4f^2} e^{2i\theta} \hat{U}_n = \frac{1}{2}\left(\frac{\omega}{f} - 1\right) e^{2i\theta} \hat{U}_n \tag{41}$$

Combining (41) with the clockwise rotating velocity of amplitude $\tilde{U}_n$ reproduces an ellipse with the correct properties. Thus (36) is a general expression relating the properties of the local near-inertial frequency velocity ellipse to the horizontal second derivatives of the complex inertial amplitude.

2.5.4. *Other forced motions.* Although these equations do not contain high-frequency internal waves, they do contain subinertial forced motions, including wind forced Rossby waves. These are described by U_G and (31). Although these are not of concern here, it is interesting to note that for very low frequencies of wind forcing the time integral in (31) will become large, and the curl of the wind stress will become the dominant forcing term, as expected [*Gill*, 1982, equation (9.10.18)].

3. APPLICATION TO STORM RESPONSE

3.1. *What is a "Storm"?*

D'Asaro [1985*b*] used equation (34) along with a linear damping as in (1) and (2) to estimate the energy flux into mixed layer inertial currents. Using many years of wind data, he found that the energy input was highly intermittent. Inertial motions were mostly generated during infrequent "storms," each of which produced a large response in the ocean, separated by long periods of "calm." It is therefore useful to consider the response of the ocean to one such storm as done by G84. The total wind-forced near-inertial wave field is then the sum of a number of such events. The results of *D'Asaro* [1985*b*] suggest that several dozen storms per year would account for most of the wind-forced energy.

3.2. *Inertial Pumping*

3.2.1. *Physics.* The initial near-inertial response of the ocean to wind forcing can be described in terms of inertial "pumping" of the deep ocean by mixed layer inertial currents [*Price*, 1981; G84; *Greatbatch*, 1984]. Inertial currents $\tilde{U}_F$ forced by the wind are confined to the mixed layer, as described by the function $Z(z)$. If these currents have a horizontal variation, vertical velocities will be generated throughout the water column with an amplitude given by the integration of (9):

$$w(z) = -\int_0^z \nabla_H \cdot \tilde{U}_F \, dz \tag{42}$$

That is, inertial frequency convergences and divergences in the mixed layer will "pump" the thermocline down and up at the inertial frequency. These displacements of the thermocline, given by ξ, where $\xi_t = w$, will produce hydrostatic pressure variations given by the integration of (8):

$$P = -\int N^2 \xi(z) dz \tag{43}$$

That is, inertial frequency pressure variations will be induced by the inertial frequency "pumping." These pressure variations are computed by combining (42) and (43) to yield (12); the integral operator $\mathbf{I}$ is merely the combination of the two integrals in (42) and (43). Inertial frequency velocities $\tilde{U}$ are accelerated by gradients of these pressures according to the momentum equations (6) and (7). The rate of acceleration, from (35), is

$$\frac{\partial \tilde{U}}{\partial t} = -\frac{i}{2f} \mathbf{I} \nabla_H^2 \tilde{U}_F \tag{44}$$

Equation (44) provides a succinct description of the initial transfer of energy from mixed layer inertial currents to the interior: horizontal variations in mixed layer inertial currents $\tilde{U}_F$ lead to inertial "pumping" of the thermocline and acceleration of inertial currents $\tilde{U}$ throughout the water column.

3.2.2. *Vertical profiles.* For an initially quiescent ocean the inertial velocity field at small times is, from (44),

$$\tilde{U} = \tilde{U}_F(t) Z(z) - \left[\frac{i}{2f}\int_0^t \nabla_H^2 \tilde{U}_F(t) dt\right] \mathbf{I} Z(z) \tag{45}$$

The velocity field is the sum of the directly wind-forced component $\tilde{U}_F$ and the inertially pumped component proportional to $\nabla_H^2 \tilde{U}_F$. These two terms have very different depth dependences. This is illustrated in Figure 1, in which it is assumed that

$$\begin{aligned} N^2(z) &= 0 & z &> -H \\ N^2(z) &= N_0^2 e^{(z+H)/b} & z &< -H \end{aligned} \tag{46}$$

with $H = 50$ m, $b = 1000$ m, $N_0 = 5 \times 10^{-3}$ s^{-1} (3 cph), and $B = 5000$ m. The directly forced component varies as $Z(z)$ (Figure 1*b*, solid curve) and is large only in the mixed layer. The inertially pumped component varies as $\mathbf{I}Z(z)$ (Figure 1*b*, dashed curve), which, although larger in the upper ocean, has a finite value at all depths. A sample velocity profile at finite time is shown in

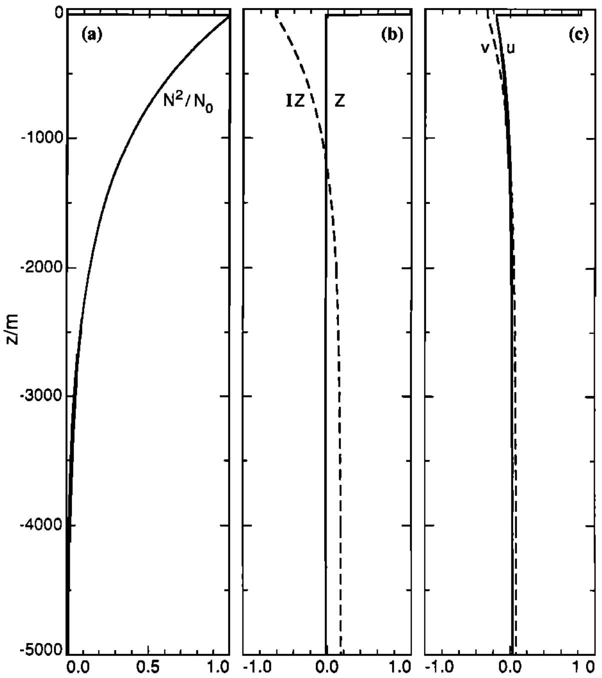

Fig. 1. Vertical structure of simulated wind-forced inertial motions assuming N^2 profile shown in Figure 1(*a*). Figure 1(*b*) shows the vertical structure of motions directly forced by the wind (Z, solid curve) and of their initial evolution (IZ, dashed curve). Figure 1(*c*) is a typical velocity profile with $u = Z + \sin(0.53)\,\mathrm{I}Z$ (solid curve) and $v = \cos(0.53)\,\mathrm{I}Z$ (dashed curve).

Figure 1*c*, in which the bracketed term in (45) is equal to $0.5e^{0.53\,i}\,\tilde{U}_F$. Inertial motions are now present both in the mixed layer and at depth. Inertial pumping has transferred energy from the mixed layer to depth.

Several characteristics of the velocity profiles (Figure 1*c*) are notable. The inertial velocity is uniform through the mixed layer, jumps sharply across the mixed layer base, and then decays with depth in the thermocline, resulting in a velocity maximum immediately below the mixed layer base. The thickness of this maximum is set by the stratification. For stratifications that include a thin seasonal thermocline, the velocity maximum is thinner and thus more distinct than that in Figure 1*c*. Examples of this pattern for various stratifications can be seen in the work of *Rubenstein* [1983], G84, *D'Asaro* [1985*a*], and *Kundu* [1986]. It should be noted that since I Z has no discontinuity across the mixed layer base, the infinitely thin shear layer at the mixed layer base is unchanged. As the mixed layer velocity vector changes, the same vector change occurs immediately below the mixed layer, so the shear is unchanged. This can be seen both in Figure 1*c* and in the references just cited.

3.2.3. *A Rossby radius.* The strength of the velocity induced by inertial pumping is proportional to the ratio of the horizontal scale of the mixed layer inertial currents to a Rossby radius L_I, defined by

$$\mathrm{I}Z(0) = \frac{L_I^2}{f^2} \qquad (47)$$

where L_I is a length scale. For the stratification (equation (46)), $L_I^2 = HbN_0^2/(2f^2)$ if, in addition, $H \ll b \ll B$. This yields $L_I \approx 7$ km. If the normal mode decomposition (equation (16)) is made and, from G84,

$$Z(z) = \sum_{n=1}^{\infty} \sigma_n p_n \qquad (48)$$

then

$$L_I^2 = \sum_{n=1}^{\infty} \sigma_n \frac{c_n^2}{f^2} p_n \qquad (49)$$

so that L_I is a weighted average of the Rossby radii $c_n f^{-1}$ associated with the normal modes. With G84's stratification, (49) yields L_I = 8.8 km. The first mode alone yields a value 80% of this, showing its dominant role in inertial pumping.

The acceleration due to inertial pumping can now be written

$$\frac{\partial \tilde{U}_0}{\partial ft} = -i\, L_I^2 \nabla_H^2 \tilde{U}_F \qquad (50)$$

where $\tilde{U}_0$ is the inertial current induced by inertial pumping at $z = 0$.

3.2.4. *Energetics.* Inertial pumping generates velocities below the mixed layer. The energy in these motions is given by

$$E_{\text{therm}} = \int_{-B}^{-H} \frac{1}{2} |\tilde{U}|^2 dz \qquad (51)$$

The potential energy contribution for near-inertial motions is small, of order ε in this analysis. For the stratification (46)

$$E_{\text{therm}} = \frac{1}{4} b\, |\tilde{U}_0|^2 \qquad (52)$$

For comparison, the energy contained in mixed layer inertial currents is

$$E_{ml} = \frac{H}{2} |\tilde{U}_F|^2 \qquad (53)$$

3.2.5. *Range of validity.* The perturbation expansion (equation (25)) used here requires that $\tilde{U}$ change very little in time f^{-1}, that is, that it be a function of the slow time τ. Applied to (50), this requires that $L_I^2 \nabla_H^2 \tilde{U}_F$ be small compared with $\tilde{U}_F$ or that the scale of the mixed layer inertial currents be large compared with L_I. The expressions for inertial pumping presented here therefore will be valid only for mixed layer inertial currents with scales of many tens of kilometers, or wavelengths greater than 150 km or so. Smaller-scale variations will generate internal waves with frequencies significantly above f and therefore require the full linear equations.

Expression (50), giving the rate of inertial pumping, is quantitatively valid for short times, when $\tilde{U}_0$ is small compared with $\tilde{U}_F$. The expression should become qualitatively incorrect as soon as the lowest mode begins to propagate away from the generation region, approximately the time given by (3) according to G84.

3.3. *Estimation of Decay Time for Mixed Layer Inertial Currents*

We now come to the key part of the paper, the estimation of the decay time for mixed layer energy by inertial pumping. One decay time will be defined as the time it takes for E_{therm} (equation (52)) to equal E_{ml} (equation (53)). A second, following G84, is based on the separation of the lowest mode.

Equations (45) and (35) clearly show that the evolution rate depends on the horizontal scale of the mixed layer inertial currents $\tilde{U}_F$. In the introduction three mechanisms that may set this scale are introduced. The scale may be set (1) by the spatial variability of the wind field, (2) by the rate at which it translates over the ocean, or (3) by the β effect. We will evaluate a decay time for each mechanism and then, in section 4, evaluate their relative importance using high-resolution wind fields.

3.4. *Decay Time and Horizontal Scale Set by the Wind*

D'Asaro [1985*b*] found that storms that generate mixed layer inertial motions usually translate across the ocean. A reexamination of 77 of the storms analyzed by *D'Asaro* [1985*b*, Figures 8–10] finds a mean translation speed of about 15 m s^{-1} with a standard deviation of about 6 m s^{-1}. At these speeds, the storms travel 100 km in only a few hours. In this time, their large-scale structure generally changes very little. It is thus useful, at least for the purposes of this paper, to assume that the storms move unchanged across the ocean. Similar assumptions are commonly made in the analysis of meteorological data on these spatial scales [*Bond and Fleagle*, 1985].

With an advection speed C in the $+x$ direction, the wind stress field can be written

$$\tau(x,y,t) = \tau(x-Ct,y,0) \tag{54}$$

The directly forced inertial motions are thus proportional to $e^{-ift + ik_A x}$ so that

$$\nabla_H^2 \tilde{U}_F = -\left(\frac{f}{C}\right)^2 \tilde{U}_F + \frac{\partial^2 \tilde{U}_F}{\partial y^2} \equiv -k_A^2 \tilde{U}_F - k_y^2 \tilde{U}_F \tag{55}$$

where $k_A = fC^{-1}$ is the wave number due to advection and k_y is a wave number associated with the y variation of $\tilde{U}_F$.

The wind thus contributes to the variability of the mixed layer inertial currents $\tilde{U}_F$ in two distinct ways. Wind stress variations in the cross-advection (y) direction generate variations in $\tilde{U}_F$ represented here by k_y. This is the first mechanism discussed in the introduction. The classic example of this is a slowly moving hurricane in which the size of the hurricane sets the spatial scale of the inertial motions [*Price*, 1983; *Greatbatch*, 1984]. The advection of the storm in the x direction introduces scale, k_A^{-1}, the distance the storm moves in time f^{-1}. This is the second mechanism discussed in the introduction. The classic example is the translating, two-dimensional front analyzed by *Kundu* [1986] and applied to data by *Kundu and Thompson* [1985] and *D'Asaro* [1985*a*]. For such a front, k_A sets the spatial scale of the inertial motions.

The essential physics of inertial pumping in both cases is retained by assuming

$$\nabla_H^2 \tilde{U}_F = -k_F^2 \tilde{U}_F \tag{56}$$

so that k_F^2 locally describes the variability introduced into the mixed layer inertial currents by the wind.

Using (50) gives the inertially pumped currents

$$\tilde{U}_0 = -iftL_l^2 k_F^2 \tilde{U}_F \tag{57}$$

so that $E_{\text{therm}} = E_{ml}$ at

$$ft_F = \left[\frac{2H}{b}\right]^{1/2} \frac{1}{L_l^2 k_F^2} \tag{58}$$

For $k_F = (100\,\text{km})^{-1}$, $t_F = 7$ days at 50°N if (46) is used. Note that the thermocline inertial currents grow linearly, so E_{therm} grows quadratically. The energy transfer rate is therefore not constant but increases with time, at least for short times.

If a modal expansion is used, G84 shows that the mixed layer inertial current amplitude is reduced by a fraction σ_1 in the time that it takes for the first mode to rotate ½π away from a pure inertial oscillation. This yields expression (3). For $k_F = (100\,\text{km})^{-1}$, $t_1 = 5$ days at 50°N using the stratification of G84. Noting that L_l^2 is similar in magnitude to $c_1^2 f^{-2}$, we see that (3) and (57) are very similar expressions, the main difference being that (57) contains information on the evolution of all the modes at short times, rather than just one. Both, however, are adequate to estimate the approximate time scale of inertial pumping when the horizontal scales of the inertial currents are set by the wind.

3.5. *Decay Time and Horizontal Scale Set by* β

Another horizontal scale, and consequently another time scale, for inertial pumping appears when β is added. Consider the evolution of inertial motions that are set up by a rapidly moving, large-scale storm with little small-scale structure. The mixed layer inertial currents directly forced by this storm, $\tilde{U}_F$, will have the same amplitude and phase over a large region. Then k_F will be very small, the inertial currents will evolve only very slowly, and little transfer of energy to the thermocline will initially occur. Now consider the same forcing, but include the variation of f as function of latitude so that $f(y) = f + \beta y$. The mixed layer inertial currents now vary as

$$\tilde{U}_F(y,t) = \tilde{U}_F(y,0)e^{-i(f+\beta y)t} \tag{59}$$

Even if $\tilde{U}_F$ is uniform at $t = 0$, its phase becomes a function of latitude for $t>0$, corresponding to a north-south wave number βt. At 50°N this equals $(100\,\text{km})^{-1}$ for t = 6.6 days, allowing inertial pumping to proceed rapidly thereafter. When (59) is substituted into (50), the acceleration due to inertial pumping is seen to be proportional to $L_l^2\beta^2 t^2$ at $z = 0$ and the inertial currents proportional to $L_l^2\beta^2 t^3/3$.

Formally, the solution to (35) for short times with $\tilde{U}_F$ constant and $\tilde{U}$ zero at $t = 0$ is

$$U = \tilde{U}_F e^{-i(f+\beta y t)}\left[Z(z) - i\frac{\beta^2 t^3}{6f}\mathbf{I}Z(z)\right] \tag{60}$$

where the second term gives $\tilde{U}_0$, the inertial pumping at $z = 0$. Computing E_{therm} (equation (51)) and equating it to E_{ml} (equation (53)), we find the decay time for mixed layer inertial currents,

$$ft_\beta = \left[\frac{18H}{b}\right]^{1/6}\left[\frac{R^2}{L_l^2}\right]^{1/3} \tag{61}$$

which has a value of about 82, or 13 inertial periods, at a latitude of 50° N. Thus horizontal scales induced by β alone can rapidly produce the small scales necessary to pump inertial energy into the thermocline.

Notice that the thermocline currents grow as t^3 here and thus the thermocline energy grows as t^6. Practically, this implies that inertial pumping is nearly negligible for times much less than t_β and then rapidly begins transferring energy at a high rate.

The characteristic wave number due to the β effect is βt. It will be important, compared with the characteristic wave number k_F imposed by the wind, if it becomes larger than k_F in the time t_F defined by (58). This implies that k_F must be larger than

$$k_\beta = \left[\frac{2H}{b}\right]^{1/2}\frac{1}{L_l^2 R} \tag{62}$$

The value of k_β is $(94\,\text{km})^{-1}$ at 50° N. For $k_F \gg k_\beta$ the β effect will have little influence on the initial decay rate of mixed layer inertial currents. For $k_F \ll k_\beta$ it will have a large effect.

If a modal decomposition is made, the evolution of mode n is given by

$$\tilde{U}_n = \tilde{U}_F e^{-i\beta y t}\left[1 - i\frac{c_n^2\beta^2 t^3}{6f}\right] \tag{63}$$

Again following G84, an evolution time can be estimated as the time for the second term to equal ½π for the first mode. This yields

$$ft_{\beta 1} = \left[3\pi \frac{f^2R^2}{c_1^2}\right]^{1/3} \quad (64)$$

which is equal to 15 inertial periods, or 10 days, using G84's stratification.

4. Simulation of Inertial Currents Using Seasat Wind Fields

4.1. *Wind Fields*

The theory developed above introduces three factors that may influence the horizontal scales of wind-forced inertial currents, namely, the horizontal scales of the wind field, the advection speed of the wind field, and the β effect. Below, the relative importance of these three factors is estimated using wind stress fields measured by the Seasat scatterometer. These data are nearly the only available wind fields with a spatial resolution better than 100 km, as is required for this problem. At this spatial resolution, no information on the time evolution of the wind is available. An approximate advection speed for the synoptic scale features described by these fields can, however, be estimated both from standard surface charts and from successive scatterometer passes. The simulations have therefore been driven by advecting the Seasat scatterometer wind fields over the ocean at a constant speed. Although this may not well represent all aspects of the time evolution, it is sufficient for the limited goals of this study.

4.2. *Simulation Techniques*

Wind stress fields were computed using data from the Seasat scatterometer [*Brown*, 1986]. Estimates of the 10-m wind from the Jet Propulsion Laboratory (Pasadena, California) were edited for attenuation, and one of the four possible directions was chosen as described by *Levy and Brown* [1986]. These were converted to estimates of surface wind stress using the formula of *Large and Pond* [1981] with no correction for boundary layer stratification. This results in a slightly irregular, gappy array of surface stress estimates with a spacing of about 50 km (Figure 2*a*).

The model requires a smoothly varying estimate of $\tau(x, y)$ so that (34) can be evaluated. In addition, some smoothing is required to reduce noise in the wind estimates. Two-dimensional smoothing splines [*Wahba*, 1984] were used to accomplish both tasks. These fit a smooth function $f(x, y)$ with continuous first derivatives to n data points $f_i(x_i, y_i)$ to minimize

$$\frac{1}{n}\sum_{i=1}^{n}[f_i - f(x_i, y_i)]^2 + \lambda^2 J(f) \quad (65)$$

where $J(f)$ is an isotropic sum of second derivatives of f that measures its smoothness. This criterion is isotropic (unlike that for bicubic splines) and therefore imposes no asymmetries on the fitted function. The relative balance between the smoothness of the fit and the closeness of the data to the surface is controlled by the parameter λ. A value of $\lambda = 1000$ m is used here. This value yields an rms difference between the raw and smoothed stress fields somewhat larger than the official error estimates for the scatterometer, 1.6 m s^{-1} in wind speed and 16° in direction [*Born et al.*, 1982]. Typically, about 20–30% of the stress field variance was removed by this method. The two components of τ were independently smoothed using this technique. An example of the resulting wind stress field is shown in Figure 2*b*.

The wind fields from a Seasat pass over the eastern North Pacific on September 11, 1978, are used here. These were chosen because they cover the low and cold front of a strong cyclone and because the same data have been previously analyzed for their meteorological content [*McMurdie and Katsaros*, 1985]. Each section of data used was small enough that the advection speed was approximately constant, and large enough to encompass a well-defined portion of the storm.

For each wind stress field and advection vector C, $\tilde{U}_F$ was computed using (34) along paths through the data parallel to C and ending at $t = 0$. The value of f corresponding to the final point was used throughout. The value of $\nabla^2\tilde{U}_F$ was estimated by evaluating $\tilde{U}_F$ on a 25-km grid and fitting a quadratic surface to all points within a 50-km radius of each grid point. Estimates of $\tilde{U}_0 ft)^{-1}$ (equation (57)), k_F, and t_F were computed at $t = 0$ using $L_l = 7$ km.

4.3. *Results*

4.3.1. *Response to a low.* Figures 2 and 3 show the simulated inertial response to a Seasat wind field measured at 0900 UT September 11, 1978. The stress field (Figures 2*a* and 2*b*) shows a well-defined cyclone with the largest winds in the northeast and southeast quadrants. Warm and cold fronts from *McMurdie* [1983] have been drawn in Figure 2*a*. As expected, the wind stress varies on a scale of several hundred kilometers.

Mixed layer inertial currents are generated by advecting this stress pattern in the direction indicated in Figure 2*c*. The resulting field of data can be interpreted either as a space-time map, with the time scale given on the right side of the data, or as a true spatial pattern, bearing in mind that f is constant in the advection direction. The variation of the complex inertial amplitude $\tilde{U}_F$ is shown in Figure 2*c*; the corresponding currents $\tilde{U}_F e^{-ift}$ are shown in Figure 2*d*.

In Figures 2*c* and 2*d*, inertial currents are generated by the changes in wind stress associated with the two wind stress maxima. The largest inertial amplitudes occur on the right side of the cyclone because the winds are strongest in this region and because the clockwise rotation of the winds with time corresponds to the clockwise rotation of inertial currents and thus evokes a resonant response [*Price*, 1981]. As expected, the inertial currents $\tilde{U}_F$ show several spatial scales. In the advection direction, they rotate with a wave number k_A, here about (75 km)$^{-1}$. In the cross-advection direction they vary with a dominant scale of several hundred kilometers, approximately that of the wind stress, as well as on smaller scales that can be traced to smaller-scale variations in the wind stress. For example, the 90° shift in inertial current direction that occurs at about 152°W, 45.5°N can be traced to a subtle change in the direction of the wind stress in the southeast quadrant of the storm combined with a decrease in the magnitude of the wind stress in the northeast quadrant of the storm.

The cross-advection scales can be seen more clearly in Figure 3, which shows a number of variables at $t = 0$. As discussed above, $\tilde{U}_F$ (Figure 3*a*) shows both a broad, several hundred kilometer variation and smaller-scale fluctuations. The 90° change in the direction of $\tilde{U}_F$, for example, appears between 300 km and 400 km. In Figure 3*b* the acceleration due to inertial pumping $\tilde{U}_0(ft)^{-1}$ (equation (57)) shows two scales. On the scale of several hundred kilometers, $i\tilde{U}_0$ mimics the behavior of $\tilde{U}_F$. For example, at 300 km the imaginary part of $\tilde{U}_F$ (dashed) is minimum, as is the real part of $\tilde{U}_0(ft)^{-1}$ (solid). This is due to the contribution of $k_A^2\tilde{U}_F$ to $\nabla_H^2\tilde{U}_F$ (equation (55)). In addition, $\tilde{U}_0(ft)^{-1}$ varies on smaller scales because of the contribution of the wind stress variations in the cross-advection direction associated with the cyclone (i.e., k_y) to ∇_H^2. The turning of $\tilde{U}_F$ between 300 km and 400 km, for example, produces a negative peak in

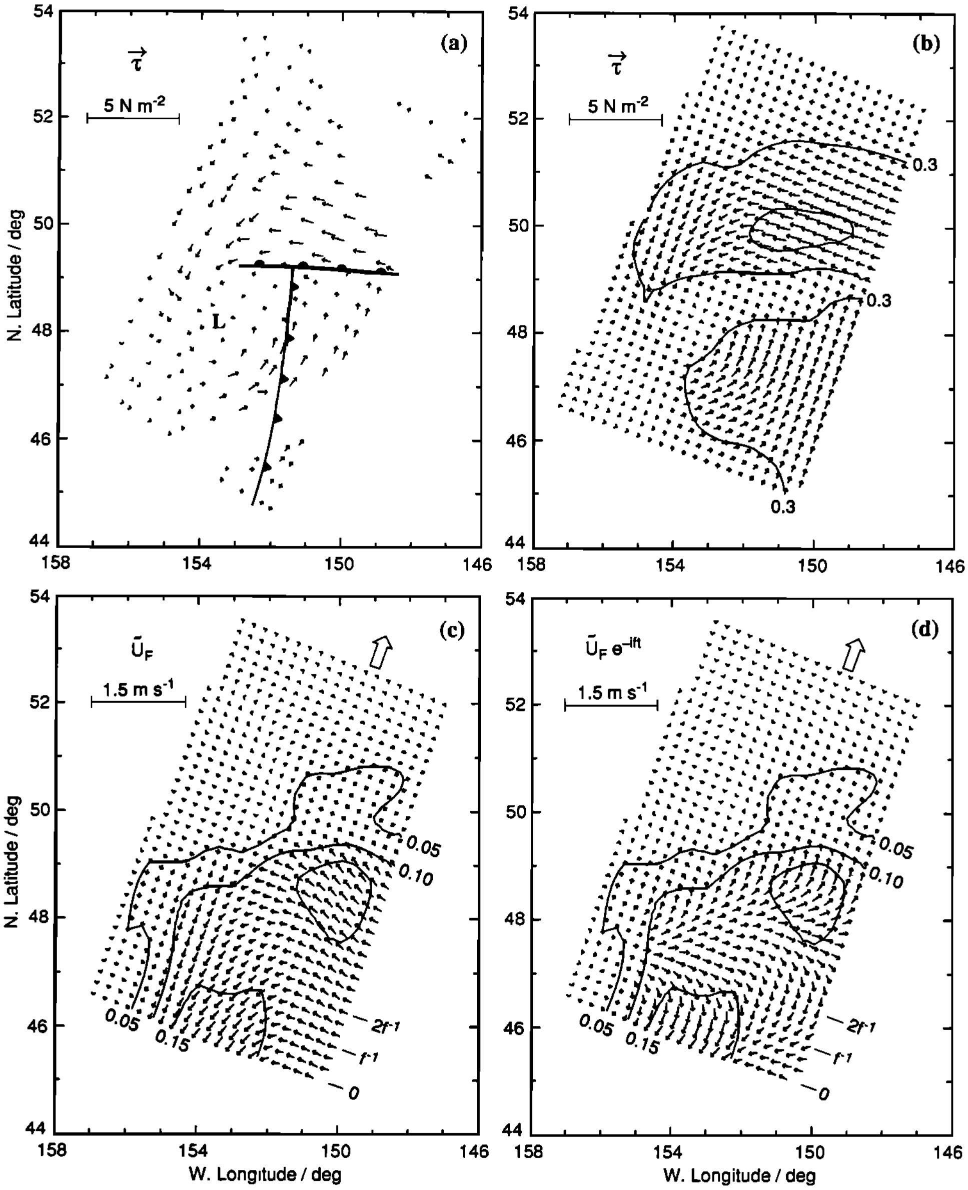

Fig. 2. Simulation using Seasat scatterometer winds from 0900 UT September 11, 1978. (*a*) Dealiased surface stress vectors. Locations of fronts and lows are indicated. (*b*) Smoothed wind stress field sampled on a 25-km grid with superimposed contours of wind stress magnitude. (*c*) Complex inertial amplitude of wind-forced motions, $\tilde{U}_F$. Advection direction and corresponding time axis are indicated. (*d*) Inertial currents corresponding to Figure 2(*c*).

$\tilde{U}_0(ft)^{-1}$. Significant energy appearing near the Nyquist wave number suggests that the scatterometer noise may be significant in this calculation.

Figure 3*c* plots t_F (equation (58)), its value assuming $k_y = 0$, and t_β (equation (61)). Note that t_F varies spatially owing to the spatial variation in k_y. The turning of $\tilde{U}_F$ between 300 km and 400 km, for example, produces a value of t_F that is more than a factor of 2 below its $k_y = 0$ value. Wind stress fluctuations in the cross-advection direction are clearly important here. Generally, however, t_F is only about 25% below the $k_y = 0$ line, which indicates that wind stress fluctuations in the cross-advection direction are only marginally important. Typically, t_β is about a factor of 2 more than t_F, indicating that the β effect will have only a small influence on the initial rate of inertial pumping.

4.3.2. *Effect of advection speed.* Figures 4 and 5 show the result of decreasing the advection speed from the observed 8.4 m s^{-1} to 4.0 m s^{-1}, which corresponds to a decrease in k_A from about 85 km to about 40 km. Since there is, in general, less variance in the wind stress at smaller scales [*Freilich and Chelton*, 1986], the inertial amplitudes are decreased (compare Figures 2 and 4). However, the biggest change is a concentration of inertial motions into a small region. At this location the two wind maxima are separated by about one wavelength, $2\pi k_A^{-1}$, resulting in a coherent forcing of the inertial motions. We might expect that the change in advection speed would increase k_A while leaving the fluctuations in the y direction unchanged. This would decrease t_F by about a factor of 4 and thus decrease the relative importance of the y fluctuations and β. Comparing Figures 3*c* and 5*c*, we note that t_F decreases as expected, but its deviation from the $k_y = 0$ value is about the same. The concentration of inertial motions into a small region has increased the small-scale variability of the inertial motions more than simple scaling arguments would sug-

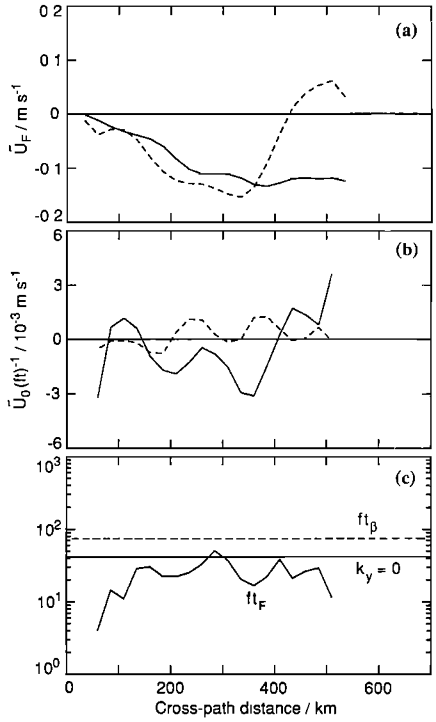

Fig. 3. Simulated quantities at $t=0$ for Figure 2. (*a*) Real (solid curve) and imaginary (dashed curve) components of $\tilde{U}_F$. (*b*) Same but for $\tilde{U}_0$, the thermocline inertial currents. (*c*) Time for energy to be transferred from mixed layer to thermocline by the β effect alone (t_β), by storm advective scales alone ($k_y = 0$), and by all wind scales (t_f).

gest. This should serve as a warning that mid-latitude storms are sufficiently complex that these simple scalings may be misleading.

4.3.3 *Response to a cold front.* Figures 6 and 7 show the simulated response to the cold front associated with the same storm. The wind stresses (Figure 6*a*) shift sharply from northeast to northwest at the front, which is drawn to coincide with the location of the wind shift. The strongest winds (Figure 6*b*) occur behind the front. Inertial currents (Figure 6*c*) are generated primarily by the frontal wind shift. North of about 48°N (y less than 300 km in Figure 7) the wind shift and the wind stress are weak. The associated inertial currents are also weak, and the estimated inertial acceleration $\tilde{U}_0(ft)^{-1}$ is noisy. At about 48°N (300 km) the frontal stress increases, leading to larger inertial currents. The change produces low values of t_F near 400 km (Figure 7*c*). From about 47°N to 45°N (450 to 650 km) the frontal wind stresses change gradually, resulting in a nearly linear change in $\tilde{U}_F$ and larger values of t_F. South of 44°N (600 to 800 km) the wind stresses behind the front increase, resulting in a turning of $\tilde{U}_F$, larger values of $\tilde{U}_0(ft)^{-1}$, and a decrease in t_F.

This front is moving fast (17.8 m s^{-1}), so the advective wave number is small, $k_A \approx (180\,\mathrm{km})^{-1}$, and the decay time due to k_A alone is quite long, approximately $200f^{-1}$. Accordingly, k_y is larger than k_A over most of the domain. The fluctuations in wind stress in the cross-advection direction are dynamically far more important than the advection speed. The β effect is also important; t_β is comparable to t_F.

On a typical weather map a cold front appears as a nearly straight line, which suggests that fluctuations of the wind stress in the along-front direction are unimportant. Such a map has a resolution of a few hundred kilometers, so the scales relevant for inertial motions cannot be resolved. The front simulated in Figure 7 is not a linear feature since fluctuations in the cross-advection direction cannot be neglected. This should serve as a warning that models of inertial pumping that treat fronts as one-dimensional wind discontinuities [*Kundu*, 1986; *Kundu and Thompson*, 1985] may be neglecting much of the variability in the wind field.

4.3.4. *Scatterometer errors.* The preceding analysis uses smoothed versions of the scatterometer data. The amplitude of the small-scale wind variations depends on the degree of smoothing applied. Here the amount of variance removed by the smoothing is comparable to the official estimates of scatterometer accuracy. However, the scatterometer is probably less accurate in regions of precipitation and unsteady winds [*Brown*, 1986], exactly the conditions under which it is being used here. The quantification of the amount of extra error and its nature is not available. A second source of error can be seen in Figure 6*a*, in which the frontal line zigzags as it passes obliquely through the lines of data. This is an aliasing effect due to a mismatch of the scatterometer footprint and its spatial resolution. Finally, the ocean is driven by wind stress, not wind. Currently, the ability of the scatterometer to measure wind stress is poorly known, and the ad hoc scheme used here for computing stress from scatterometer wind is subject to an unknown error. Nevertheless, the data used here appear to be sufficiently accurate to show the importance of all three factors, k_A, k_y, and β, in determining the decay time of mixed layer inertial currents. Until the errors are better understood, it will be difficult to do quantitative work using scatterometer data on the spatial scales of interest here.

5. SUMMARY OF RESULTS

A set of equations describing the linear evolution of internal gravity waves of near-inertial frequency in a horizontally homogeneous ocean is derived using an asymptotic perturbation analysis that is uniformly valid in time. These equations are used to estimate the decay time for mixed layer inertial motions generated by mid-latitude storms due to the transfer of energy to inertial motions at deeper levels. The transfer rate depends on the

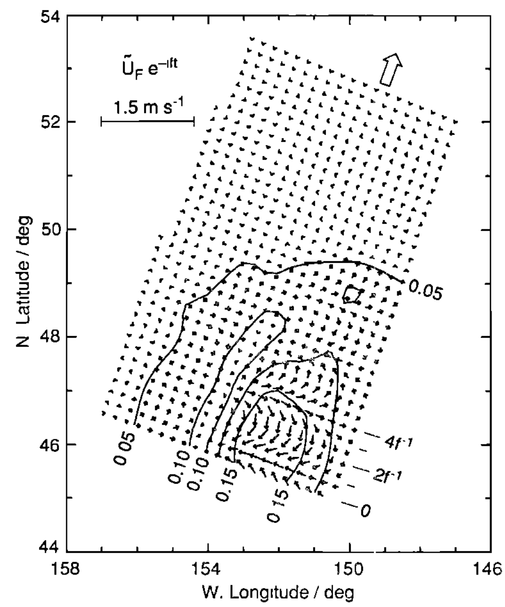

Fig. 4. Same as Figure 2(*d*), but with slower advection speed.

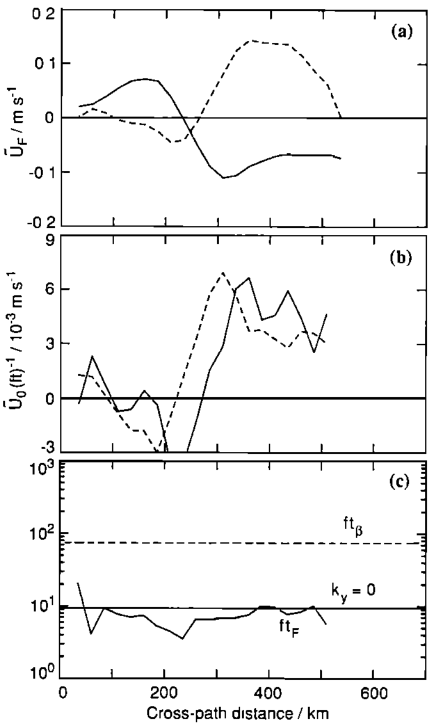

Fig. 5. Simulated quantities at $t = 0$ for Figure 4. Format and symbols are the same as in Figure 3.

stratification and on the horizontal scales of the inertial motions. If the storm is assumed to advect over the ocean while its structure is slowly changing, three factors govern the horizontal scales of the inertial motions:

1. The advection speed of the storm, C, imposes a wave number of magnitude $k_A = Cf^{-1}$ in the advection direction.
2. Fluctuations of the wind stress in a direction perpendicular to the advection direction impose wave numbers oriented perpendicular to the advection direction.
3. A new result is that the north-south variation in f imposes a time dependent north-south wave number of magnitude βt where $\beta = \partial f / \partial y$.

Characteristic energy transfer times for each factor are given in (58) and (61). Factors 1 and 2 depend on some aspect of the wind stress and thus require a detailed knowledge of the wind stress field on scales smaller than 100 km for their evaluation. Factor 3, in contrast, is independent of the wind field and thus imposes an approximate upper limit on the residence time of inertial motions in the mixed layer, typically 1–2 weeks.

Simulations of storm-forced inertial motions using wind stress fields derived from the Seasat scatterometer indicate that any one, or more, of these three factors can be important, depending on the storm and one's location within it.

6. DISCUSSION

6.1. *Estimating the Decay Time for Mixed Layer Inertial Oscillations*

As discussed in the introduction, the excitation of mixed layer inertial currents by wind stress has been observed numerous times and is well understood. It appears that the subsequent decay of these currents can be modeled using linear near-inertial wave theory, but this requires a horizontal scale of the mixed layer inertial currents of the order of 100 km or, equivalently, a hor-

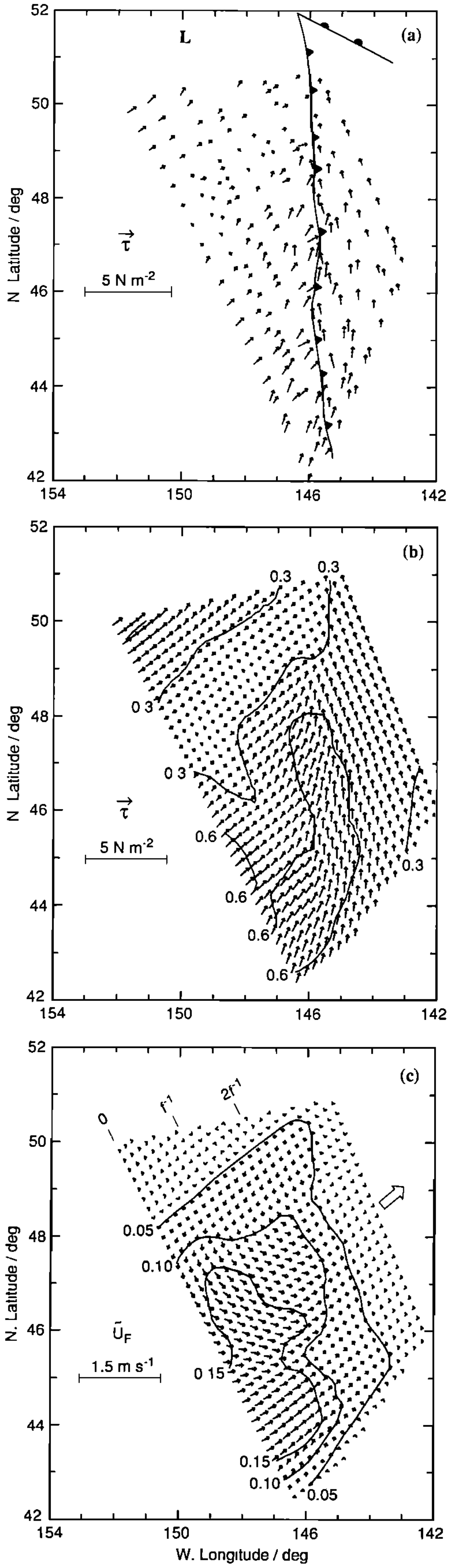

Fig. 6. Simulation of response to a cold front using Seasat scatterometer winds from 1840 UT September 11, 1978. Format and symbols in Figures 6(*a*)–6(*c*) are the same as in Figure 2.

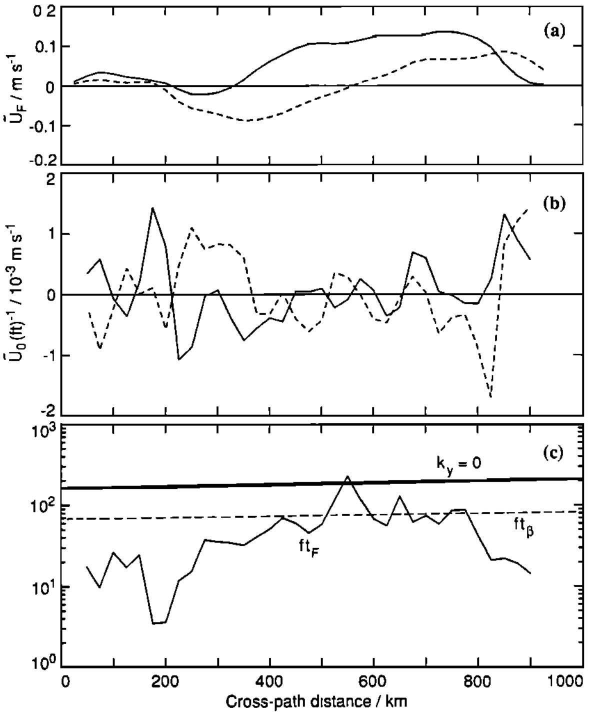

Fig. 7. Simulated quantities at $t = 0$ for Figure 6. Format and symbols are the same as in Figure 3.

izontal wavelength of order 600 km. This scale may be set by the wind, by preexisting oceanic variability, or, as introduced in this paper, by the β effect. Of these, only the β effect will operate at all times; the storm scales depend on the storm characteristics, and the intensity of the oceanic mesoscale varies greatly. The decay time imposed by the β effect, therefore, places an upper limit of 1–2 weeks on the residence time of storm-forced inertial oscillations in the mixed layer. This is in accord with existing observations; storm-forced inertial oscillations do not persist for much longer than this in any observations known to the author.

The present study indicates that scales imposed by the wind are often as important as those imposed by β. The accurate modeling of their effect, however, requires wind stress fields with a spatial resolution better than 100 km and a temporal resolution better than a few hours. Such data are not currently available even to researchers, let alone for use in operational or large-scale models. It thus seems unlikely that a wind stress field of sufficient resolution for routinely modeling the decay of mixed layer inertial oscillations will soon be available. Even if such a wind field were available, however, it would only accelerate the inevitable decay of mixed layer inertial currents due to the β effect. For many purposes the difference may not matter, and a model that includes only the β effect may be sufficient.

6.2. *The Usefulness of Scatterometer Wind Fields*

The simulation of wind-forced inertial motions probably requires wind stress fields with a resolution better than 100 km. Satellite scatterometry appears to be the only method of obtaining such data routinely, but our current understanding of the errors in scatterometer wind stress measurements is poor. Accordingly, it will be difficult to use scatterometer data properly in upper ocean models until the measurement errors are better understood. The wind stress fields used in this work were generated by a meteorology student (G. Levy) studying scatterometry for his dissertation. Clearly, easier ways of distributing future scatterometer data will be required if such data are to be applied to oceanographic problems without a similar effort.

6.3. *Two- and Three-Dimensional Inertial Motions*

Many simple models of the forcing of near-inertial motions have been used in previous studies. These generally lead to a two-dimensional wave field for short times. If, for example, the scale associated with advection is dominant, the mixed layer inertial motions will be uniform in the direction perpendicular to the direction of advection. This is the case studied by *Kundu and Thompson* [1985]. If the small-scale structure of the wind field is dominant, the wave field will be uniform in the advection direction. This is the case studied by G84. If the β effect is dominant, the wave field will be uniform in the east-west direction. At long times, β will always become important [G84] and north-south scales will appear in the problem.

In each of these limiting cases the wave field is two-dimensional and considerable simplification occurs [*Kundu*, 1986; *Kundu and Thompson*, 1985]: $\tilde{U}_F$, for example, will always be 90° out of phase with $i\nabla_H^2 \tilde{U}_F$ and thus with $\tilde{U}_0$. If more than one of the factors becomes important, as is likely for realistic wind fields, the inertial motions will no longer be two-dimensional. Then $\tilde{U}_F$ and $\tilde{U}_0$ need not have an exact phase relationship.

6.4. *Shear at the Mixed Layer Base*

The analysis here does not address the rate of evolution of inertial shear at the mixed layer base. Traditional mixed layer models [*Niiler and Kraus*, 1977] decay such shear at the same rate as they decay the velocity in the mixed layer. Such a formulation cannot be justified on the basis of the models used here, which will decay velocity and shear at different rates. The evolution of velocity is dominated by the evolution of the lowest few modes, while the evolution of shear is dominated by the higher modes. Since the high modes evolve much more slowly than the low modes, the shear changes much more slowly than the velocity. Physically, evolution of the low-mode components of an initial slab, mixed layer velocity profile, as in Figure 1*b*, results in an offset of the slab from zero, as in Figure 1*c*, without changing the magnitude of the velocity change at the mixed layer base. More attention to this distinction, and to the processes that influence shear, as opposed to velocity, is needed in future studies of mixed layer dynamics.

6.5. *The Importance of Oceanic Mesoscale Variability*

This paper has considered only the linear evolution of inertial motions in a homogeneous ocean. Under some circumstances, inhomogeneities in the ocean may play an important role in setting the horizontal scales, and thus the evolution rate, of near-inertial motions. Here, planetary scale variations in f were found to be capable of generating mesoscale variations in initially homogeneous near-inertial motions within a few tens of inertial periods. Gyre-scale and mesoscale variations in velocity may act similarly to β and generate small-scale inertial motions even more rapidly. Thus it seems possible that the horizontal scales, and thus evolution rates, of inertial motions generated within a field of strong mesoscale eddies could be set almost entirely by the characteristics of the eddies, as opposed to those of the wind field.

6.6. *The Importance of Mesoscale Meteorological Variability*

This paper makes clear the close link between inertial motions and atmospheric wind stress fluctuations on the 30- to 200-km scale. This is the domain of subsynoptic, or mesoscale, meteorology. It seems that future progress toward the understanding of inertial motions will require the cooperation of oceanographers and mesoscale meteorologists.

Acknowledgments. Scatterometer data for this work were dealiased and edited by Gad Levy. Brad Bell provided the two-dimensional spline algorithms and educated me as to their meaning. Kraig Winters helped keep the perturbation analysis of the equations of motion mathematically correct. This work was supported by the Office of Naval Research under contract N00014-84-C-0111. University of Washington School of Oceanography contribution 1778.

REFERENCES

Bond, N. A., and R. G. Fleagle, Structure of a cold front over the ocean, *Q. J. R. Meteorol. Soc., 111,* 739–759, 1985.

Born, G. H., D. N. Held, D. B. Lame, R. G. Lipes, D. R. Montgomery, P. J. Rygh, and J. F. Scott, Seasat data utilization project report, *Rep. D-36,* Jet Propul. Lab., Pasadena, Calif., 1982.

Brown, R. A., On satellite scatterometer capabilities in air-sea interaction, *J. Geophys. Res., 91,* 2221–2232, 1986.

Calman, J., On the interpretation of ocean current spectra, II, Testing dynamical hypotheses, *J. Phys. Oceanogr., 8,* 644–652, 1978.

D'Asaro, E. A., Upper ocean temperature structure, inertial currents, and Richardson numbers observed during strong meteorological forcing, *J. Phys. Oceanogr., 15,* 943–962, 1985*a*.

D'Asaro, E. A., The energy flux from the wind to near-inertial motions in the surface mixed layer, *J. Phys. Oceanogr., 15,* 1043–1059, 1985*b*.

Freilich, M. H., and D. B. Chelton, Wavenumber spectra of Pacific winds measured by the Seasat scatterometer, *J. Phys. Oceanogr., 16,* 741–757, 1986.

Fu, L.-L., Observations and models of inertial waves in the deep ocean, *Rev. Geophys., 19,* 141–170, 1981.

Gill, A. E., *Atmosphere-Ocean Dynamics,* 662 pp., Academic, San Diego, Calif., 1982.

Gill, A., On the behavior of internal waves in the wakes of storms, *J. Phys. Oceanogr., 14,* 1129–1151, 1984.

Greatbatch, R. J., On the response of the ocean to a moving storm: Parameters and scales, *J. Phys. Oceanogr., 14,* 59–78, 1984.

Gregg, M. C., E. A. D'Asaro, T. J. Shay, and N. Larson, Observations of persistent mixing and near-inertial internal waves, *J. Phys. Oceanogr., 16,* 856–885, 1986.

Hasselman, K., Wave-driven inertial oscillations, *Geophys. Fluid Dyn., 1,* 463–502, 1970.

Houze, R. A., and P. V. Hobbs, Organization and structure of precipitating cloud systems, *Adv. Geophys., 24,* 225–315, 1982.

Kervorkian, J., and J. D. Cole, *Perturbation Methods in Applied Mathematics,* Springer-Verlag, New York, 1981.

Kundu, P. K., A two-dimensional model of inertial oscillations generated by a propagating wind field, *J. Phys. Oceanogr., 16,* 1399–1411, 1986.

Kundu, P. K., and R. E. Thompson, Inertial oscillations due to a moving front, *J. Phys. Oceanogr., 15,* 1076–1084, 1985.

Kunze, E., and R. Lueck, Velocity profiles in a warm-core ring, *J. Phys. Oceanogr., 16,* 991–995, 1986.

Large, W. G., and S. Pond, Open ocean momentum flux measurements in moderate to strong winds, *J. Phys. Oceanogr., 11,* 324–336, 1981.

Levy, G., and R. A. Brown, A simple, objective analysis scheme for scatterometer data, *J. Geophys. Res., 91,* 5153–5158, 1986.

Marmorino, G. O., L. J. Rosenblum, and C. L. Trump, Fine-scale temperature variability: The influence of near-inertial waves, *J. Geophys. Res., 92,* 13,049–13,062, 1987.

McMurdie, L. A., Seasat scanning multichannel microwave radiometer (SMMR) observation of North Pacific cyclones, M.S. thesis, Univ. of Wash., Seattle, 1983.

McMurdie, L. A., and K. B. Katsaros, Atmospheric water distribution in a midlatitude cyclone observed by the Seasat scanning multichannel microwave radiometer, *Mon. Weather Rev., 113,* 584–598, 1985.

Munk, W., Internal wave spectra at the buoyant and inertial frequencies, *J. Phys. Oceanogr., 10,* 1718–1728, 1980.

Niiler, P. P., and E. B. Kraus, One-dimensional models of the upper ocean, in *Modelling and Prediction of the Upper Layers of the Ocean,* edited by E. B. Kraus, pp. 143–172, Pergamon, Elmsford, N.Y., 1977.

Overland, J. E., and J. G. Wilson, Mesoscale variability in marine winds at mid-latitude, *J. Geophys. Res, 89,* 10,599–10,614, 1984.

Paduan, J., R. DeSzoeke, and R. A. Weller, Inertial oscillations in the upper ocean during the Mixed Layer Dynamics Experiment (MILDEX), *J. Geophys. Res.,* in press, 1988.

Pollard, R. T., On the generation by winds of inertial waves in the ocean, *Deep Sea Res., 17,* 795–812, 1969.

Pollard, R. T., Properties of near-surface inertial oscillations, *J. Phys. Oceanogr., 10,* 385–398, 1980.

Pollard, R. T., and R. C. Millard, Comparison between observed and simulated wind-generated oscillations, *Deep Sea Res., 17,* 813–821, 1970.

Price, J. F., Upper ocean response to a hurricane, *J. Phys. Oceanogr., 11,* 153–175, 1981.

Price, J. F., Internal wave wake of a moving storm, I, Scales, energy budget and observations, *J. Phys. Oceanogr., 13,* 949–965, 1983.

Rubenstein, D. M., Vertical dispersion of inertial waves in the upper ocean, *J. Geophys. Res., 88,* 4368–4380, 1983.

Sanford, T. B., P. G. Black, J. R. Haustein, J. W. Feeney, G. Z. Forristall, and J. F. Price, Ocean response to a hurricane, I, Observations, *J. Phys. Oceanogr., 17,* 2065–2083, 1987.

Sherwin, T. J., Inertial oscillations in the Irish Sea, *Cont. Shelf Res., 7,* 191–211, 1987.

Smith, R., Evolution of inertial frequency oscillations, *J. Fluid Mech., 60,* 383–389, 1973.

Wahba, G., Surface fitting with scattered noisy data on Euclidean d-space and on the sphere, *Rocky Mt. J. Math., 14,* 281–298, 1984.

Webster, F., Observations of inertial-period motions in the deep sea, *Rev. Geophys., 6,* 473–490, 1968.

Weller, R. A., The relation of near-inertial motions observed in the mixed layer during the JASIN (1978) experiment to the local wind stress and to the quasi-geostrophic flow field, *J. Phys. Oceanogr., 12,* 1122–1136, 1982.

White, W. B., Vertical Reynolds stress divergence in the upper ocean associated with linear wind-driven, near-inertial waves of finite amplitude, *J. Phys. Oceanogr., 16,* 1190–1203, 1986.

E. A. D'Asaro, Applied Physics Laboratory, University of Washington, 1013 N.E. 40th Street, Seattle, WA 98105.

(Received February 13, 1988;
revised May 2, 1988;
accepted September 26, 1988.)